Synthesis of magnetron sputtered WO3 nanoparticles–degradation of 2–chloroethyl ethyl sulfide and dimethyl methyl phosphonate

3 AUTHORS:

Monu Verma
Indian Institute of Technology Roorkee
5 PUBLICATIONS **11** CITATIONS

SEE PROFILE

Ramesh Chandra
Indian Institute of Technology Roorkee
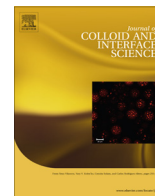**186** PUBLICATIONS **1,545** CITATIONS

SEE PROFILE

Vinod K Gupta
Indian Institute of Technology Roorkee
303 PUBLICATIONS **14,732** CITATIONS

SEE PROFILE

Synthesis of magnetron sputtered WO₃ nanoparticles-degradation of 2-chloroethyl ethyl sulfide and dimethyl methyl phosphonate

CrossMark

Monu Verma [a,b], Ramesh Chandra [b], Vinod Kumar Gupta [a,c,d,*]

[a] Department of Chemistry, Indian Institute of Technology Roorkee, Roorkee 247667, India
[b] Institute Instrumentation Centre, Indian Institute of Technology Roorkee, Roorkee 247667, India
[c] Center for Environment and Water, Research Institute, King Fahd University of Petroleum and Minerals, Dhahran, Saudi Arabia
[d] Department of Applied Sciences, University of Johannesburg, Johannesburg, South Africa

GRAPHICAL ABSTRACT
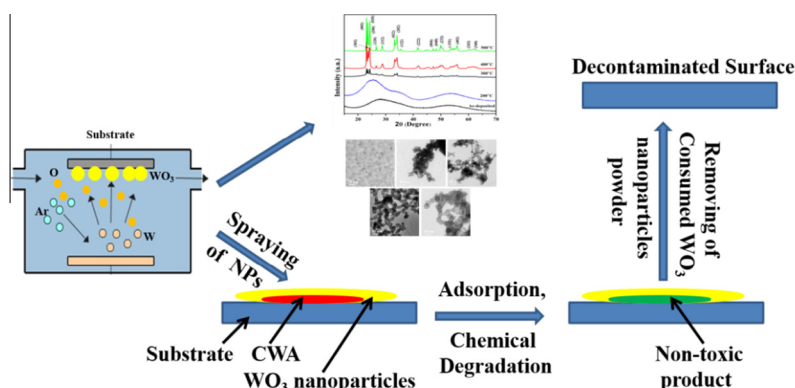
ARTICLE INFO

ABSTRACT

In the present study, tungsten oxide nanoparticles were synthesized using DC magnetron sputtering and investigated their potential for decontamination of 2-chloroethyl ethyl sulfide (CEES) and dimethyl methyl phosphonate (DMMP). The tungsten oxide nanoparticles were characterized by Powder XRD, FE-SEM, EDS, TEM, TGA, N_2-BET and FT-IR techniques. The XRD patterns of as-deposited and post annealed tungsten oxide nanoparticles reveal that the crystallite size of detected monoclinic phase WO₃ nanoparticle was increased with increasing annealing temperatures. The phase and increase in particles size of WO₃ nanoparticles were also confirmed by Raman and TEM analyses. The obtained surface area ($\sim$63–33 m²/g) of magnetron sputtered WO₃ nanoparticles was found to be enhanced significantly as compared to reported surface area of WO₃ nanoparticles synthesis by various techniques. The study of degradation reactions of CEES and DMMP on the surface of obtained nanoparticles was carried out by using GC and GC–MS techniques. The decontamination reactions were found to be pseudo first order steady state with rate constant (k) and half life values 0.143–0.109 h^{-1} and 4.82–6.49 h for CEES and 0.018–0.010 h^{-1} and 36.87–66.65 h for DMMP, respectively. The FT-IR data reveal the role of hydrolysis reactions in the decontamination of CEES as well as DMMP.

© 2015 Elsevier Inc. All rights reserved.

* Corresponding author at: Department of Chemistry, Indian Institute of Technology Roorkee, Roorkee 247667, India. Fax: +91 1332 273560.
  E-mail addresses: vinodfcy@gmail.com, vinodfcy@iitr.ac.in (V.K. Gupta).

1. Introduction

Inorganic metal oxide nanomaterials indicate intriguing adsorption and chemical reactivity toward chemical warfare agents (CWAs) [1–5]. They possess high surface area, high adsorption capacity, large number of reactive functional groups and reactive morphology which facilitate superior decontamination capacity toward CWAs and environment pollutants [6–9]. The higher surface area possesses great interest to decontaminate the CWAs by adsorption and decomposition (chemical degradation) approach.

Sulfur mustard (HD) and sarin (GB) are the well known CWAs which have been used in the first and second world war. HD acts on skin and mucous membrane and creates blisters. It also alkylates guanine nucleotide in DNA and causes fatality to the cells. GB attacks on nervous transmission and blocks it permanently by binding with acetylcholinesterase enzyme which causes paralyzes and mortality deceases. Recently, it has been misused in Japan by terrorist and in Gulf war (Iran-Iraq war) by Iraq army. Therefore, it is a great challenge for the scientific community to decontaminate these deadly CWAs in the battle field conditions for the sake of national security. For these purpose, several methods or strategies have been used for the neutralization of highly toxic CWAs. The first decontaminant used for detoxify the agents was bleaching powder and thereafter super chlorinated bleach. After the second world war, a new decontaminate DS$_2$ was developed which is more effective decontaminant to detoxify the CWAs with long term storage ability [10]. But it is quite toxic and creates corrosion to metal, fabric and human skin. Therefore, a large number of chemicals such as *o*-iodo benzoic acid, peroxides, oximes, chloramines, and beta cyclodextrin have been developed and studied as catalyst to detoxify the CWAs. But water is undesirable to decontaminate the electronic devices. Recent investigation has explored the sorbent decontaminant by which most of the above problems minimized. A sorbent decontaminant is free of liquid, solid material which have high adsorbent capacity to adsorb the liquid agent strongly in its pores and degrades eventually.

A number of various nanosized metal oxides such as MgO, CaO, Al$_2$O$_3$, ZnO, MnO$_2$ nanobelts, V$_{1.02}$O$_{2.98}$ nanotubes possess enhanced chemical reactivity toward CWAs including HD and GB and their simulants [11–16]. These metal oxides play an active role to decontaminate CWAs through hydrolysis, elimination and oxidation reactions on the surface of nanomaterials. Kleinhammes et al. have studied the degradation of 2-chloroethyl ethyl sulfide (CEES) and found that the presence of water molecules within the nanotubes gives hydrolysis reaction of CEES and converting them non-toxic form [17]. Mahato et al. also reported the decontamination of HD and CEES over the surface of MnO$_2$ nanobelts through hydrolysis reaction and mentioned the rate constant (k) values 0.01 and 0.02 h^{-1} respectively [15]. Also Singh et al. reported the decontamination of HD and CEES using V$_2$O$_3$ nanostructures through hydrolysis, elimination and oxidation reactions and found the rate constant (k) values 0.052 and 0.026 h^{-1} respectively [18]. Aurian and Boucher [19] and Kanan and Tripp [20] used metal oxides for the decontamination of DMMP through hydrolysis reaction. Verma et al. studied the decontamination of sarin on the surface of Al$_2$O$_3$ nanostructure through hydrolysis reaction and found the rate constant (k) value 0.032 h^{-1} [21]. Recently, Verma et al. reported the degradation of CEES on the surface of DC sputtered CuO nanoparticles through hydrolysis reactions with rate constant values 0.434–0.134 h^{-1} [22]. The DC sputtered CuO nanoparticles exhibited much better results in comparison to previously reported CuO nanoparticles and other metal oxides materials synthesized using chemical methods. Inspired by these results, we have chosen newer material having high adsorption capacity to degrade CWAs within few hours of duration to ensure the enhancement in the confidence levels regarding safety against the CWAs.

In the present work we have chosen tungsten oxide (WO$_3$) nanomaterials. It is an important semiconducting material having potential applications such as electrochromic or photochromic devices, gas sensors, solar energy devices, optical displays and photo catalysts [22–30]. WO$_3$ nanoparticles have been synthesized using different methods such as sol–gel, precipitation, thermal decomposition, and hydrothermal process [31–34]. Over the chemical synthesis route, physical vapor deposition (PVD) such as magnetron sputtering holds distinguishes advantages such as high purity, reproducibility, uniformity and narrow size distribution [35]. Hence, WO$_3$ nanoparticles were synthesized using DC magnetron sputtering technique under optimized conditions for the removal and detoxification of CWAs. To the best of our knowledge nobody has reported the synthesis of WO$_3$ nanoparticles using PVD technique and their use for the degradation of CWAs. In our case, the synthesized WO$_3$ nanoparticles possess higher surface area that motivate us to attempt the study of degradation of CEES and DMMP on the surface of WO$_3$ nanoparticles.

Sulfur mustard and sarin are widely used as CWAs but being highly toxic, these are not recommended for research purpose. Hence, CEES and DMMP which are less toxic than sulfur mustard and sarin and involve a low risk are widely used to carry out research. Therefore, in the present paper we report the adsorptive removal kinetics of these simulants with WO$_3$ nanoparticles synthesized by DC magnetron sputtering.

2. Experimental

2.1. Materials

The tungsten target of 99.99% purity was purchase from Testbourne Ltd, USA. The oxygen gas cylinder, dichloromethane, bis (trimethyl silyl) trifluoro acetamide and acetonitrile were obtained from E. Merck India Ltd. CEES (CH$_3$CH$_2$SCH$_2$CH$_2$Cl) and DMMP (CH$_3$PO(OCH$_3$)$_2$) of 98% purity were obtained from Sigma–Aldrich, India Ltd.

2.2. Synthesis of WO$_3$ nanoparticles

Tungsten oxide nanoparticles have been synthesized in a 12″ diameter custom designed vacuum chamber (Excel Instrument, Mumbai). The chamber consists of various ports to accommodate sputtering gun, copper cold finger arrangement to cool the substrate with liquid nitrogen (liq-N$_2$), gas line, glass window and a scraper for collecting the particles from the substrate. Sputtering was carried out using tungsten target of 2″ diameter and 5 mm thickness. The chamber was initially evacuated to 10^{-7} Torr using a turbo molecular pump backed by rotary pump. Thereafter, an optimum working pressure was maintained in the sputtering chamber with argon and oxygen gas in a specific ratio. Before acquiring the working pressure, the hollow copper cold finger was continuously filled up with liquid nitrogen (liq-N$_2$) to cool the substrate to $\leqslant -194$ °C (79 K). During sputtering, liq-N$_2$ was also continuously filled up in the copper cold finger to maintain the desired substrate temperature. The reason for keeping low substrate temperature is to inhibit the grain growth in the plane of the film leading to production of nanoparticles. Also, contamination due to the possible diffusion of atoms from the substrate with the deposited material is minimized at lower temperature. During sputtering the W atoms were sputtered from the target and react with the oxygen atoms in chamber or on the copper cold finger substrate during deposition and form WO$_3$ nanoparticles. The nanoparticles were scratched carefully at room temperature (25 °C) and then crushed in a pestle mortar to homogenize. The nanoparticles were annealed in air at temperature range of 200–

Table 1
Sputtering parameters for the synthesis of WO$_3$ nanoparticles.

Target	Base pressure	Working pressure	Gas used	Deposition time	Distance (d)	Power	Substrate temperature	Annealing temperatures
W	4.7×10^{-7} Torr	30 mTorr	Ar:O$_2$::40:10	16 h	5 cm	80 W	−194 °C	As-deposited, 200, 300, 400, 500 °C

d = distance between target and substrate.

500 °C for 3 h. Table 1 lists the sputtering parameters used for the synthesis of WO$_3$ nanoparticles.

2.3. Characterization of WO$_3$ nanoparticles

The structure and phase composition of the DC sputtered WO$_3$ nanoparticles were determined using X-ray diffractometer (Bruker AXS, D8 Advance) using Cu Kα radiation (λ = 1.541 Å). The scanning was carried out keeping 1.0 s/step with a step size of 0.02° at room temperature. The Raman spectral analysis was acquired using In via Raman analyzer of (Renishaw, United Kingdom) using 514 nm laser as an excitation wavelength. The surface morphology of WO$_3$ nanoparticles was studied using field emission-scanning electron microscope (FE-SEM, Zeiss, Ultra plus55). The elemental compositional analysis was carried out using energy dispersive spectroscopy (EDS) attached with FE-SEM. The particle size was measured using transmission electron microscope (TEM, FEI TECNAI G^2) operating at 200 kV. WO$_3$ nanoparticles were mixed with ethanol and sonicated for 30 min. to achieve the better dispersion of particles. Subsequently, a drop of the sonicated solution was placed onto a carbon coated copper grid (300 mesh size). The specific surface area and pore size distribution of the WO$_3$ nanoparticles were determined using Autosorb-1-C from Quantachrome, USA. The samples were first put under 10^{-2} Torr dynamic vacuum to remove the embedded gas from the samples for 6 h at 200 °C. Further, the samples were allowed to cool up to room temperature and subsequently N$_2$ adsorption–desorption isotherms were obtained at liq-N$_2$ temperature (77 K). The thermogravimetry analyses of synthesized WO$_3$ nanoparticles were recorded on thermogravimetric analyzer (TGA, EXSTAR 6300). Thermograms for materials were recorded in the range 25–800 °C with heating rate 10 °C/min. in the presence of nitrogen atmosphere. The degradation kinetics of CEES and DMMP were studied using gas chromatograph (Chemito 8610) equipped with the flame ionization detector (FID) and BP5 column (30 m length and 0.5 mm inner diameter). The characterization of reaction products was carried out using gas chromatograph (HP Agilent) coupled with mass spectrometer (5973 inert) equipped with HP-5 column of 30 m × 0.25 mm × 0.25 μm, USA make. The degradation product was also characterized through Fourier transform infrared spectroscopy (FT-IR, Nicolet NEXUS Aligent 1100) in the range 400–4000 cm^{-1} using KBr disks.

2.4. Reaction procedure

The reaction of CEES or DMMP was carried out on the surface of WO$_3$ nanoparticles to understand the decontamination capacity of the synthesized material. For this purpose, 100 μl solution of dichloromethane (DCM) having 5 μl of CEES was added to 100 mg WO$_3$ nanoparticles in seven separate test tubes of equal size and then stirred for 2 min to ensure uniform mixing. The DCM was used to facilitate the uniform distribution of agent molecules (CEES or DMMP) within the bulk powder. The remaining agents were extracted with the help of acetonitrile within a time interval of 1 h, 2 h, 4 h, 6 h, 8 h, 16 h and 24 h to study the kinetics of degradation. The remaining agents were extracted by using 5.0 ml of acetonitrile for five times (each time 1 ml) in order to complete extraction. Extracted solutions were quantitatively analyzed by gas chromatograph equipped with flame ionization detector in the programming mode from 120 to 250 °C at a rate of 10 °C/min by calibrating the concentrations. The injection port and detector port were kept at 240 and 250 °C, respectively. The concentration of extracted solutions was calibrated with standard solutions for accurate quantification. The experiments were repeated more than six times in order to ensure the accuracy of the kinetics results.

3. Results and discussion

3.1. Characterization of WO$_3$ nanoparticles

Fig. 1 shows the XRD patterns of as-deposited and annealed WO$_3$ nanoparticles. The XRD patterns show that crystallinity of the WO$_3$ nanoparticles increased with increasing the annealing temperature. The XRD peaks of as-deposited and annealed (at 200 °C) nanoparticles have large full width at half maxima (FWHM) resulting overlap of peaks and hence nanoparticles exhibited XRD amorphous nature. On the other hand as the annealing temperature increased to 300 °C and above, the peaks are clearly separated due to increased crystalline nature of WO$_3$ nanoparticles. The higher crystallinity indicates the smaller FWHM and increment in particle size. It was observed that the nanoparticles show monoclinic phase (JCPDF file no. 01-072-0677) with (002), (020) and (200) preferred crystallographic orientation of the peaks at 23.08°, 23.58° and 24.32° of 2θ values, respectively. However, at 400 °C, one additional peak was found at 24.08° and assigned to (303) plane of W$_{20}$O$_{58}$ (JCPDF file no. 00-005-0386). The average crystallite size of the annealed nanoparticles was calculated using Debye–Scherer formula. It has been observed that the particle size of WO$_3$ nanoparticles increased (9–47 nm) with annealing temperature. Maximum size (∼47 nm) nanoparticles were obtained after annealing at 500 °C in open atmosphere. No other XRD peak due to any impurity was observed from the XRD pattern and which clearly indicates the formation of high purity WO$_3$ nanoparticles. To confirm the structure phase of as-deposited nanoparticles Raman spectra was carried out as
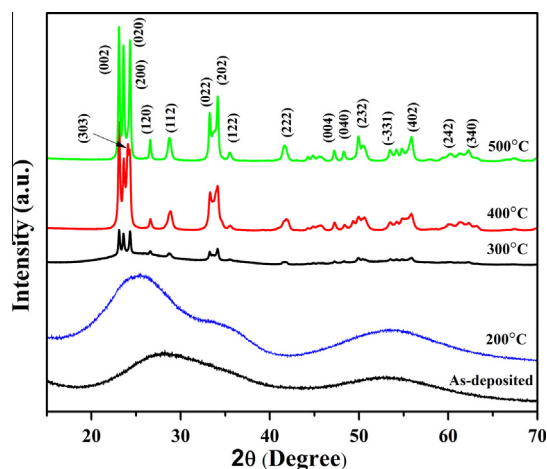
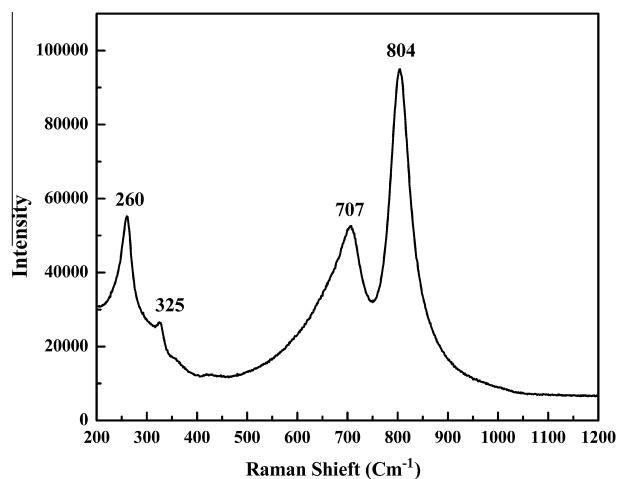**Fig. 1.** XRD patterns of WO$_3$ nanoparticles.

Fig. 2. Raman spectra of as-deposited WO_3 nanoparticles.

Fig. 4. EDS spectra of as-deposited WO_3 nanoparticles.

shown in Fig. 2. It can be seen from Fig. 2 that WO_3 nanoparticles have two regions at 200–400 and 600–900 cm^{-1}. The Raman peaks observed at lower wave numbers 260 and 325 cm^{-1} indicating the bending modes of O—W—O. The higher wave number peaks at 707 cm^{-1} are due to O—W—O vibration and at 804 cm^{-1} are corresponding to crystalline WO_3 stretching vibration mode of bridging oxygen of W—O—W. These two peaks clearly attributes to the formation of monoclinic phase of WO_3 nanoparticles [36,37]. Fig. 3 represents the FE-SEM images of as-deposited and annealed WO_3 nanoparticles. It has been observed from FE-SEM images that the annealed nanoparticles are less agglomerated as compare to as-deposited WO_3 nanoparticles. Moreover, the particle size and size distribution of WO_3 nanoparticles increase continuously with increasing annealing temperature from 200 to 500 °C. The increase in particle size with annealing temperature is attributed to the merging of grains and smaller nanoparticles into neighboring
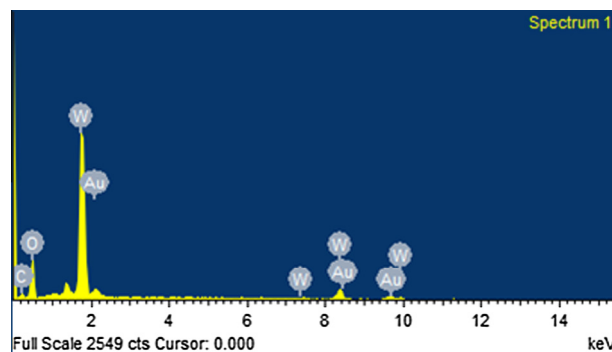
bigger particles [22,38]. The EDS spectra of as-deposited WO_3 nanoparticles are shown in Fig. 4. Spectra clearly reveal that WO_3 nanoparticles are in the proper stoichiometric ratio of W and O toward 1:3. The Au and C signals are coming due to gold coating and double sided tape used during the EDS analysis. No other elements can be detected which indicate the synthesis of high purity WO_3 nanoparticles. Fig. 5 shows the TEM images of the as-deposited and annealed WO_3 nanoparticles. The TEM images indicate the spherical type morphology of WO_3 nanoparticles. Table 2 lists the size of nanoparticles as calculated from TEM images. It is clear that the particle size increases as the annealing temperature raised from 200 to 500 °C. The selected area electron diffraction (SAED) of the as-deposited WO_3 nanoparticles is shown in Fig. 6. The ring patterns appeared for as-deposited nanoparticles clearly indicate that the nanoparticles are highly polycrystalline with principally rings of (002), (120), (122) and (222) which match very well with the XRD results of WO_3 nanoparticles. Thus XRD, Raman, FE-SEM, EDS and TEM analyses clearly indicate the formation of monoclinic phase WO_3 nanoparticles with high purity and narrow size distribution.
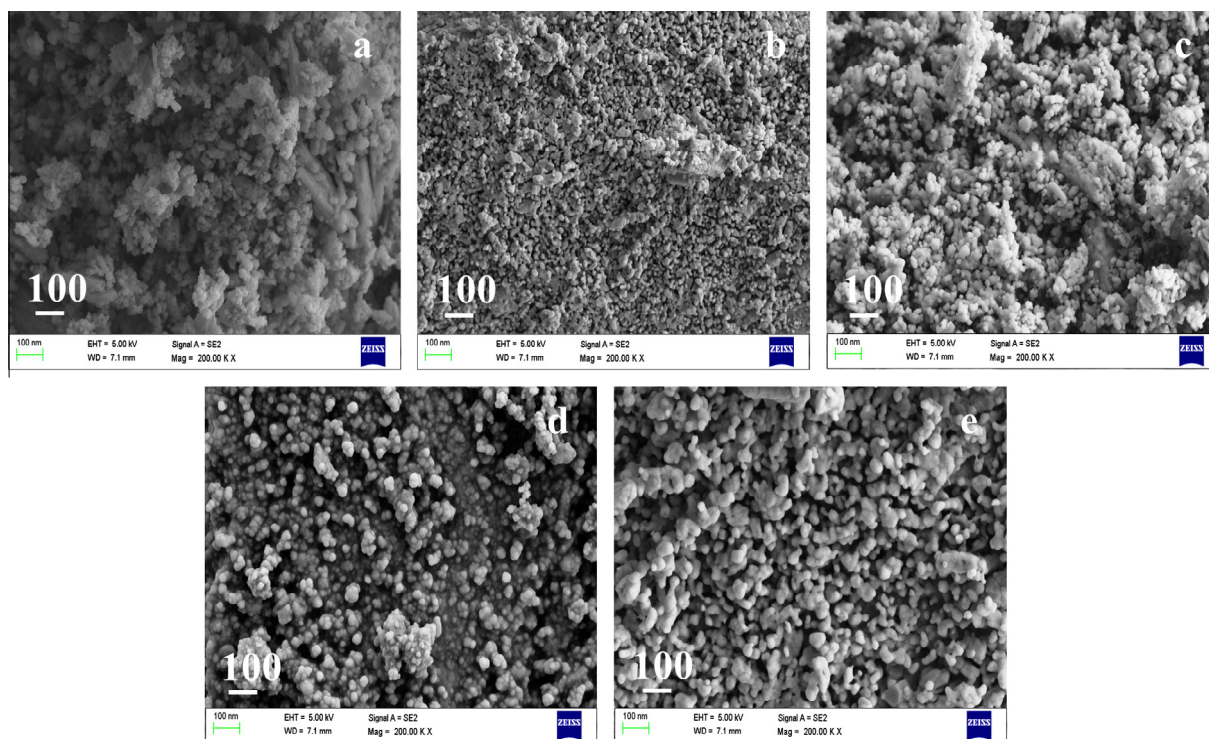

Fig. 3. FE-SEM images of tungsten oxide nanoparticles (a), as-deposited and annealed at (b) 200 °C, (c) 300 °C, (d) 400 °C and (e) 500 °C.
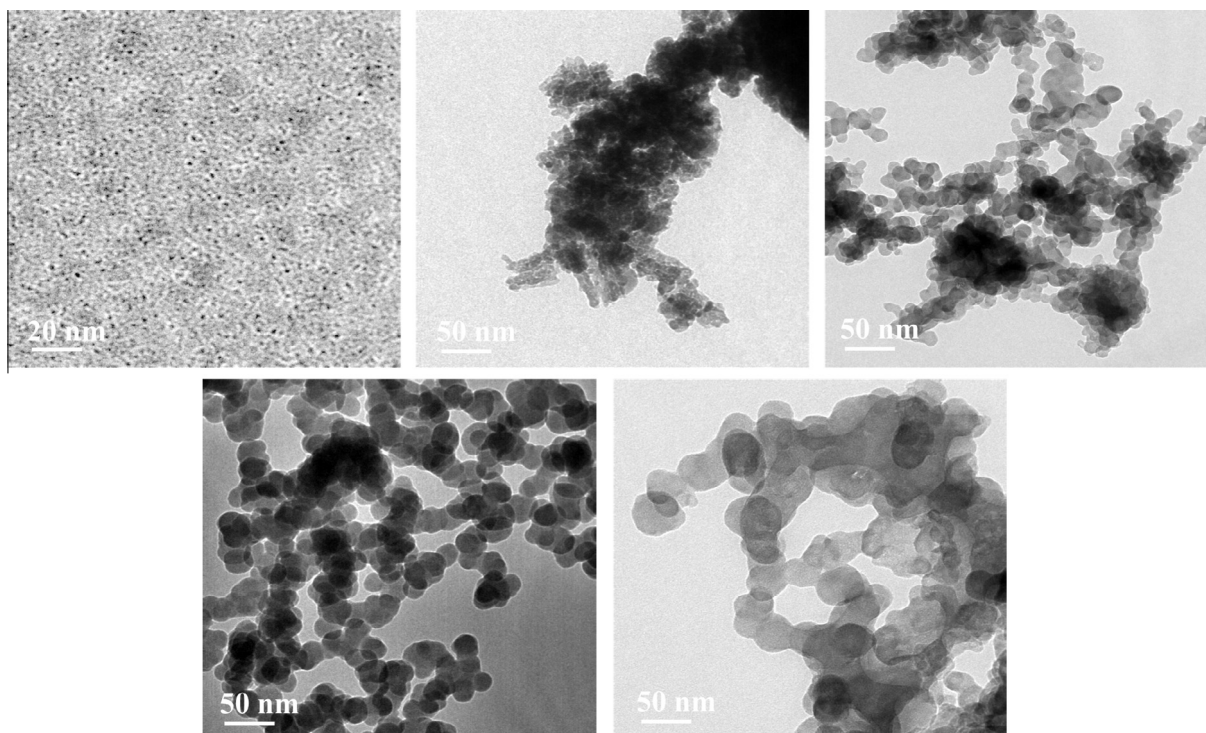
Fig. 5. TEM images of CuO nanoparticles (a), as-deposited and annealed at (b) 200 °C, (c) 300 °C, (d) 400 °C and (e) 500 °C.

Table 2
Particle size, surface area, pore volume, and WO₃ nanoparticles of as-deposited and annealed at different temperatures.

	Annealing temperature of WO$_3$ (°C)				
	As-deposited	200	300	400	500
Particle size	2	9	21	36	47
Surface area (m^2/g)	63.22	54.90	50.89	40.28	33.28
Pore volume (ml/g)	0.128	0.118	0.111	0.101	0.082

Fig. 7. Adsorption–desorption isotherm of as-deposited WO₃ nanoparticles.

The surface area and pore size distribution of WO₃ nanoparticles were carried out by using Brunauner–Emmet–Teller (BET) and Barrett–Joyner–Halenda (BJH) methods, respectively. Fig. 7 represents the N₂ adsorption–desorption isotherm of type IV and Fig. 8 shows the pore size distribution of as-deposited WO₃ nanoparticles. The obtained values of surface area and the pore volume of all the samples are given in Table 2. The obtained surface area (63.22–33.28 m²/g) of the magnetron sputtered WO₃ nanoparticles was found to be significantly higher compare to the reported surface area (1.93–16.45 m²/g) of WO₃ nanoparticles synthesized using different methods [39–41]. WO₃ nanoparticles consist of pores in the range of mesopores as depicted by pore size distribution values (Fig. 8). The calculated values of pore volume lie in the range of 0.1285–0.0821 cm³/g. The data clearly indicate that as the annealing temperature increases from 200 to 500 °C, both surface area and pore volume are decreases. These results are consistent with the reported data [25].

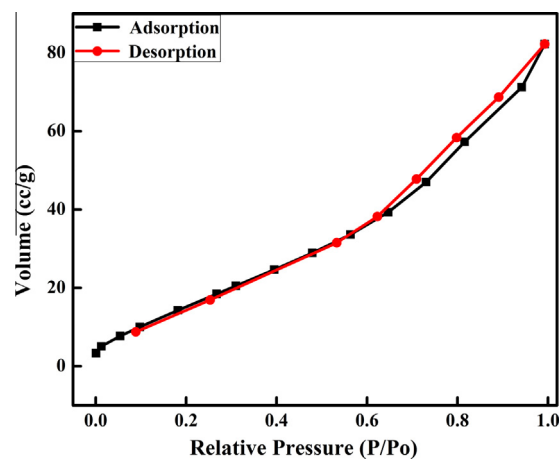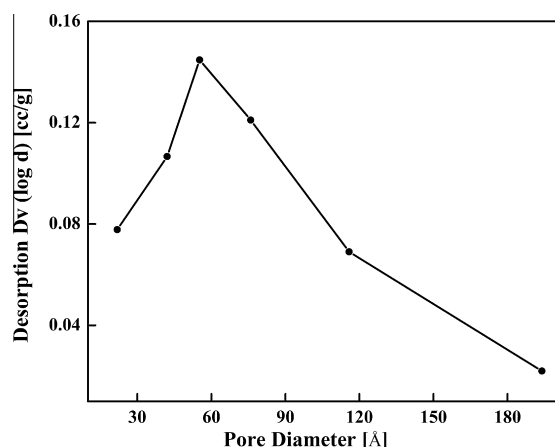**Fig. 6.** SAED pattern of as-deposited WO₃ nanoparticles showing polycrystalline rings.

Fig. 8. BJH pore size distribution of as-deposited WO$_3$ nanoparticles.

3.2. Kinetics of CEES and DMMP decontamination

In order to understand the kinetics of CEES degradation, the WO$_3$ nanoparticles of different sizes were exposed CEES for a period of 24 h. The concentration of the unreacted CEES was extracted from the reaction mixture by using acetonitrile at a specific interval of time. The concentration of unreacted CEES was find out by GC–FID. Subsequently the obtained kinetics data were plotted by taking the concentration on Y-axis and time on X-axis. Smooth curves occur in the exponential decreasing order of CEES with time for all reaction (not shown here). Whereas linear plots observed by taking the log of unreacted CEES on Y-axis and time on X-axis, depicting the pseudo first order kinetics as shown in Fig. 9(a) and results are consistent with the reported data [2,42]. The kinetic plots indicate that the concentration of CEES for all the samples decreases with time. Also kinetic reaction seems to be fast in the initial stage and a study state occurs at the later stage of the reaction. The values of rate constant and half life were lie in the range of 0.143–0.109 h^{-1} and 4.82–6.49 h, respectively shown in Table 3. DMMP also reacted in a similar way indicating the exponential decrease of concentration with time (not shown here) and linear curves as shown in Fig. 9(b). The values of rate constant and half life were found to be in the range of 0.018–0.010 h^{-1} and 36.87–66.65 h, respectively for all samples as shown in Table 3. The above data clearly indicate that the reactivity of WO$_3$ nanoparticles

Table 3
Results of degradation of CEES and DMMP on the surface of different sizes WO$_3$ nanoparticles.

	Particle size of CuO nanoparticles (nm)				
	2	9	21	36	47
Kinetic rate constant, (K) h^{-1} of CEES	0.143	0.133	0.126	0.113	0.109
Half life (t$_{1/2}$) h of CEES	4.82	5.18	5.46	6.11	6.49
Kinetic rate constant, (K) h^{-1} of DMMP	0.018	0.015	0.013	0.011	0.010
Half life (t$_{1/2}$) h of DMMP	36.87	45.01	50.23	58.25	66.65

toward DMMP exhibited pseudo first order kinetics behavior [15,43]. From the GC data it is clearly revel that CEES and DMMP degrade 98 and 53.4% on the surface of as-deposited and it decreases up to 91.8% and 40.7% as the particle size increases after annealing. The fast initial reaction is probably due to rapid adsorption and distribution of the liquid within the pores and its interaction with the accessible reactive sites and hydroxyl groups. When the sites are exhausted, the limited surface reaction occurs obviously, replacing the initial fast reaction by the steady state reaction [43–46]. The values of the rate constant (k) and half life (t$_{1/2}$) of the degradation of CEES and DMMP on the surface of WO$_3$ nanoparticles of different sizes were calculated by using the first order rate equation i.e. $k = 2.303 \times$ slope and $0.693/(2.303 \times$ slope) respectively and are given in Table 3.

It is clear from the experimental results that the rate of degradation of CEES and DMMP decreases as the particle size increases i.e. smaller particles give high degradation efficiency compare to larger particles. The probable reason for the decrease in degradation rate is due to increase in the particle size is the surface area. The DC-sputtered WO$_3$ nanoparticles possess higher surface area ($\sim$63–33 m^2/g) compared to previously reported WO$_3$ nanoparticles synthesized by others methods which lie in the range of $\sim$1–16 m^2/g as given above. These higher surface areas seemed to have imparted more adsorption capacity toward CEES and DMMP. Due to large adsorption capacity of WO$_3$ nanoparticles, CEES and DMMP were found to be rapid adsorption followed by its distribution within their pores and react with the reactive sites of synthesized nanoparticles and convert them into non-toxic form. Also, decrement in the surface area with increasing particle size leads to reduction in the adsorption capacity. Gu et al. reported that variation in annealing temperature bought about change in surface structure and hence the surface acidic and redox properties [47].
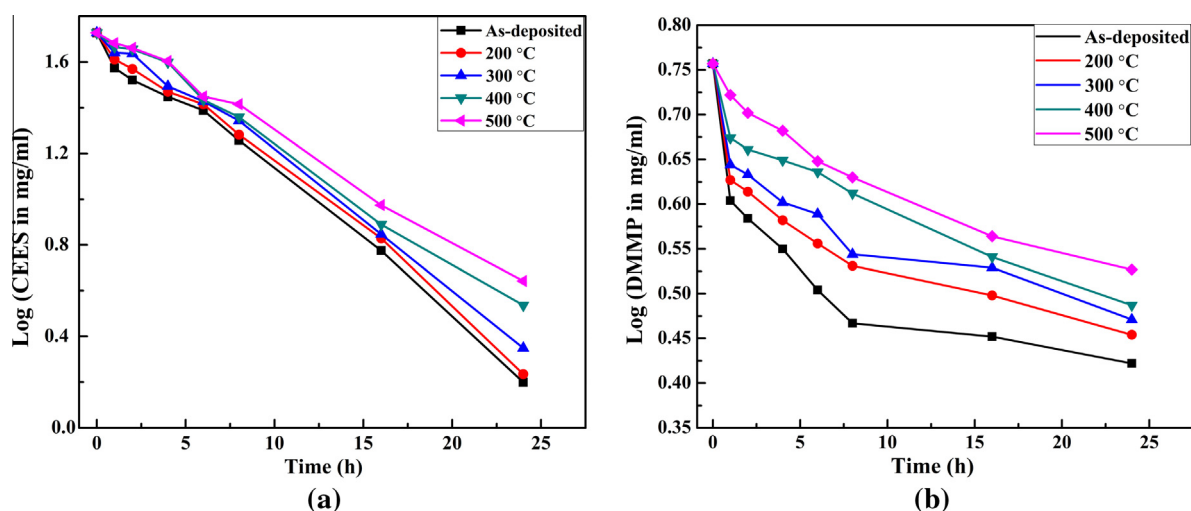

Fig. 9. Kinetics of degradation of (a) CEES and (b) DMMP on the surface of WO$_3$ nanoparticles.

Tang and co workers reported that degradation of CWAs was not only depends on the surface acidic and basic properties of metal oxides but also amount of adsorbed water [48]. The rate of degradation of CWAs profited through hydrolysis reaction with increasing of water content i.e. positive effect of water found for degradation of CWAs. With increasing the annealing temperature, the particle size increases (agglomeration) as observed in FE-SEM and TEM studies due to which surface area of the synthesized material decreases. Literature also indicates that surface area decreases with increasing annealing temperature due to further growth of particles [25]. Due to decrease in surface area with increasing particle size, the available active sites for the adsorption and the activation of the reactant decreases which in turn reduces the rate of degradation reaction.

No excess of water was added to the WO_3 nanoparticles, whatever moisture adsorbed from the atmosphere while transferring the samples along with other reactive functionalities seems to have facilitated the decontamination. The WO_3 samples were subjected to TGA in order to check the amount of water present on the surface of them. The TGA pattern of as-deposited WO_3 nanoparticles is shown in Fig. 10. It was observed that the moisture get entrapped into the WO_3 nanoparticles during expose to the atmosphere. From TGA graph, it is clear that WO_3 nanoparticles show weight loss 9.37% up to 250 °C and no further weight loss was observed up to 800 °C. This weight loss is only due to desorption of physisorbed water. Data also reveal that WO_3 nanoparticles of 2, 9, 21, 36, 47 nm sizes have a weight loss of 9.96%, 7.09%, 4.45%, 1.73%, and 1.63%, respectively. So, it is clear that with increase in particle size through annealing temperature, the amount of physisorbed water/hydroxyl group on the surface of WO_3 nanoparticles decreases due to which weight loss decreases. The results are consistent with the reported results [49].

3.3. GC–MS analysis

The extracted reaction mixtures were analyzed using GC–MS and FT-IR in order to understand the reaction mechanism and the products formed during the degradation. Since hydrolysis products of CEES and DMMP have polar and non-volatile nature due to which they were derivatized before GC–MS analysis. For all the samples, GC–MS data indicate the m/z values at 178, 163, 103, 89, and 73. These m/z values clearly reveal the formation of hydrolysis product of CEES i.e. hydroxyl ethyl ethyl sulfide (HEES), emphasizing the role of WO_3 nanoparticles in hydrolysis reaction for decontamination CEES to HEES thereby rendering

Fig. 10. TGA patterns of as-deposited DC sputtered WO_3 nanoparticles.

them to non-toxic form. Moreover, FT-IR data for all the samples that were exposed to CEES reveal that the band intensity at 700 cm^{-1} of C—Cl disappeared and, change of peak pattern at around 1440 and 1295 cm^{-1} of (CH_2—Cl) occurs. Another one peak occurs of small increase in intensity at 3411 cm^{-1} of (—O—H). These observations confirm the hydrolysis of CEES on the surface of WO_3 nanoparticles and formation of HEES.

Based on the above GC–MS and FT-IR data, the reaction mechanism for the decontamination of CEES on the surface of WO_3 nanoparticles is proposed in Fig. 11(a). According to the above scheme, CEES molecules reacted with WO_3 nanoparticles in two ways. In one way, they reacted with physisorbed or intercalated waters molecules which were present on the surface of WO_3 nanoparticles to form HEES in which cyclic sulphonium ion seemed to be formed as shown in Fig. 11(a). This cyclic sulphonium ion is formed due to attack of sulfide on the β carbon atom of CEES and is considered as SN1 reaction. Since sulphonium ion is highly unstable due to which it could not be extracted out and detected by GC [50]. Subsequently sulphonium ion undergoes hydrolysis reaction with water molecules adsorbed by WO_3 nanoparticles (no more water was added to the reaction) giving rise to the formation of HEES. In second way, CEES molecules reacted with isolated hydroxyl group (W—OH) and Lewis acid (W^{6+}) sites to form surface bound alkoxy species. The mechanism and results are consistent with the previously reported results [45,48,51].

Subsequently, the formation of silylated hydrolysis product of DMMP i.e. methyl phosphonic acid (MPA) (m/z = 240, 225, 194, 147, 133, and 73), emphasized the role of hydrolysis reaction in the decontamination of DMMP to form non-toxic product. In addition to this, in FT-IR data, the bands present at 1275 cm^{-1} (P=O) and 1020 cm^{-1} (P—O—C) of DMMP disappeared. One band at 1234 cm^{-1} indicates the interaction of P=O with the surface functional group of WO_3 nanoparticles. Another peak occurs at 3411 cm^{-1} indicating the presence of —OH group. These observations confirm the formation of MPA on the surface of WO_3 nanoparticles surface through hydrolysis reaction.

Based on the GC–MS and FT-IR data, the reaction mechanism for the degradation of DMMP on the surface of WO_3 nanoparticles is proposed in Fig. 11(b). As per this, DMMP molecules reacted with similar way as in case of CEES. In one way they reacted with physisorbed or water molecules to form MPA (non-toxic products) and in another way, they reacted with isolated hydroxyl group (W—OH) and Lewis acid (W^{6+}) sites to form surface bound phosphonates. The mechanism and results are consistent with the previous reported data [14,15,21,52]. Overall hydrolysis reactions occur on the surface of WO_3 nanoparticles with formation of surface bound alkoxy or surface bound phosphonates which facilitated the decontamination of CEES and DMMP and rendering them non-toxic. Collectively, the WO_3 nanoparticles synthesized by DC magnetron sputtering offer large values of surface area which facilities faster adsorption and encapsulation of CEES and DMMP, physisorbed waters, isolated hydroxyl group, Lewis acid (W^{6+}) sites to make toxic agents as non-toxic. The synthesized DC sputtered WO_3 nanoparticles give better reaction rate constant values than earlier reported sorbent decontaminants such as Fullers earth, mesoporous MnO_2, and V_2O_3 nanotubes [15,18]. These materials exhibited relatively lower reactivity toward CEES and decontaminate it less than 90% with rate constant (k) values ~0.02–0.026 h^{-1} in comparison to the presently synthesized WO_3 nanoparticles which degraded CEES up to 98% with rate constant (k) values 0.143–0.109 h^{-1}. Also, in case of DMMP, WO_3 nanoparticles presently synthesized give effective rate constant (0.188–0.0104 h^{-1}) than reported earlier using activated carbon (0.008–0.020 h^{-1}) [52–66]. These results clearly showed that, DC sputtered WO_3 nanoparticles give superior results compare to existing solid decontaminants.
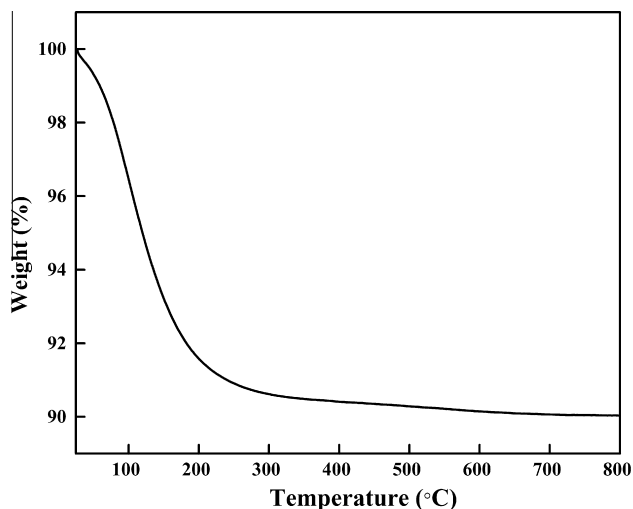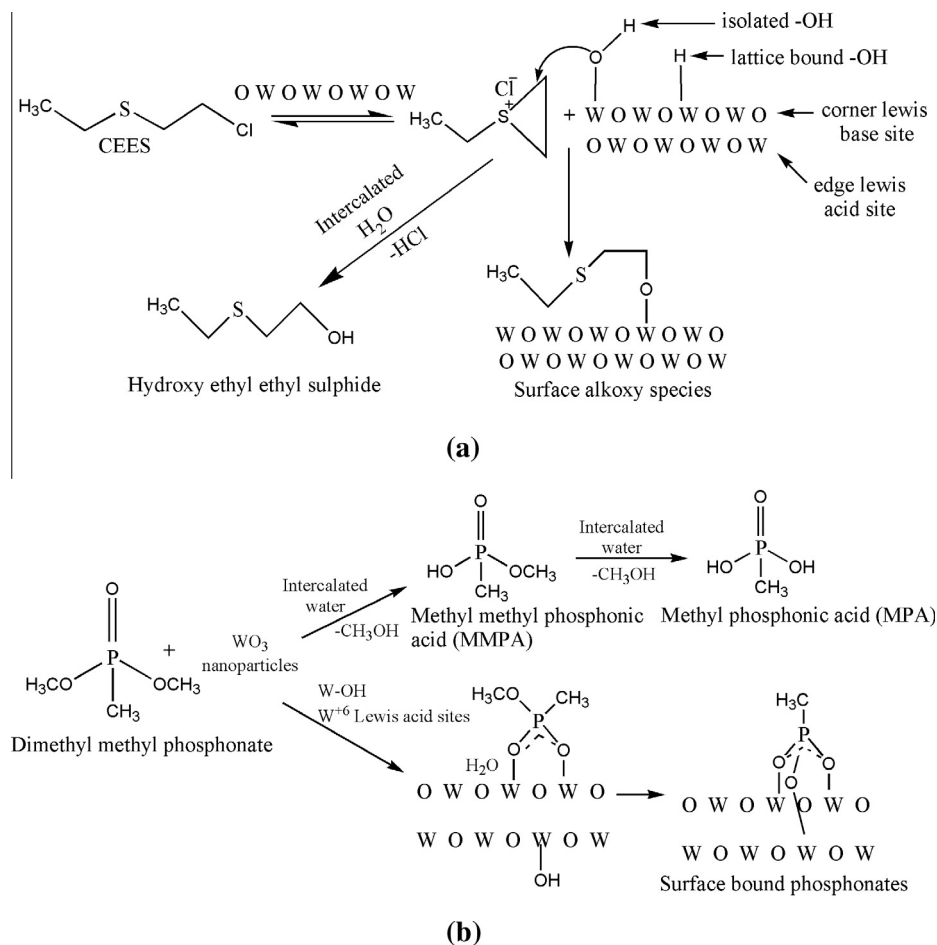
Fig. 11. Reaction scheme of (a) CEES and (b) DMMP occurring on the surface of WO$_3$ nanoparticles.

4. Conclusion

The decontamination of CEES and DMMP over various sizes WO$_3$ nanoparticles has been studied in the present work. The WO$_3$ nanoparticles have been synthesized using DC magnetron sputtering technique. Thereafter, they were annealed at different temperatures to vary the particle size. This novel PVD technique provides WO$_3$ nanoparticles of high purity with a narrow size distribution and high surface area. Due to these advantages, DC sputtered WO$_3$ nanoparticles show enhanced decontamination of CEES and DMMP over earlier studied existing solid decontaminants such as Fullers earth, mesoporous MnO$_2$, V$_2$O$_3$ nanotubes and activated carbon. The decontamination reactions exhibited pseudo first order steady state (predominantly hydrolysis) with rate constant (k) and half life ($t_{1/2}$) values 0.143–0.109 h^{-1} and 4.82–6.49 h and 0.018–0.010 h^{-1} for CEES and 36.87–66.65 h for DMMP with increase in particle size, respectively. The magnetron sputtered WO$_3$ nanoparticles (as-deposited and annealed) give superior decontamination results compare to reported literature. Among various WO$_3$ nanoparticles, as-deposited show better decontaminating results over the annealed nanoparticles. The future work will focus on the decontamination of other CWAs' simulants and photocatalytic application of these nanoparticles synthesized using DC magnetron sputtering process.

Acknowledgments

References

[1] V. Stengl, T.M. Grygar, J. Bludska, F. Oplustil, T. Nemec, Mater. Res. Bull. 47 (2012) 4291–4299.
[2] G.K. Prasad, P.V.R.K. Ramacharyulu, K. Batra, Beer Singh, A.R. Srivastava, K. Ganesan, R. Vijayaraghavan, J. Hazard. Mater. 183 (2010) 847–852.
[3] M. Winter, D. Hamal, X. Yang, H. Kwen, D. Jones, S. Rajagopalan, K.J. Klabunde, Chem. Mater. 21 (2009) 2367–2374.
[4] J.G. Ekerdt, K.J. Klabunde, J.R. Shapley, J.M. White, J.T. Yates Jr., J. Phys. Chem. 92 (22) (1988) 6182–6188.
[5] P.W. Bartram, G.W. Wagner, US Patent No. 5689038, November 18, 1997.
[6] K.J. Klabunde, J. Stark, O. Koper, C. Mohs, D.G. Park, S. Decker, Y. Jiang, I. Lagadic, D. Zhang, J. Phys. Chem. 100 (1996) 12142–12153.
[7] G.D. Sides, D.W. Mason, R.P. Seiders, Aberdeen Proving Ground, MD, October 1984, pp. 285–291.
[8] J.P. Kumar, G.K. Prasad, P.V.R.K. Ramacharyulu, P. Garg, K. Ganesan, Mater. Chem. Phys. 142 (2013) 484–490.
[9] V. Štengl, D. Opluštil, T. Nemec, Microporous Mesoporous Mater. 156 (2012) 224–232.
[10] J.B. Jacson, Development of Decontamination Solution DS2: CWLR, 2368, April 1960.
[11] J.V. Stark, D.G. Park, I. Lagadic, K.J. Klabunde, Chem. Mater. 8 (1996) 1904–1912.
[12] G.W. Wagner, O. Koper, E. Lucas, S. Decker, K.J. Klabunde, J. Phys. Chem. B 104 (2000) 5118–5123.
[13] D.B. Mawhinney, J.A. Rossin, K. Gerhart, J.T. Yates Jr., Langmuir 15 (1999) 4789–4795.
[14] T.H. Mahato, G.K. Prasad, Beer Singh, J. Acharya, A.R. Srivastava, R. Vijayaraghavan, J. Hazard. Mater. 165 (2009) 928–932.
[15] T.H. Mahato, G.K. Prasad, Beer Singh, K. Batra, K. Ganesan, Microporous Mesoporous Mater. 132 (2010) 15–21.
[16] T.H. Mahato, G.K. Prasad, Beer Singh, A.R. Srivastava, K. Ganesan, J. Acharya, R. Vijayaraghavan, J. Hazard. Mater. 166 (2009) 1545–1549.

[17] A. Kleinhammes, G.W. Wagner, H. Kulkarni, Y. Jia, Q. Zhang, L.C. Qin, Y. Wu, Chem. Phys. Lett. 411 (2005) 81–85.
[18] B. Singh, T.H. Mahato, A.K. Srivastava, G.K. Prasad, K. Ganesan, R. Vijayaraghavan, R. Jain, J. Hazard. Mater. 190 (2011) 1053–1057.
[19] B.B. Aurian, M.M. Boucher, Langmuir 5 (1989) 170–174.
[20] S.M. Kanan, C.P. Tripp, Langmuir 17 (2001) 2213–2218.
[21] A.K. Verma, A.K. Srivastava, B. Singh, D. Shah, S. Shrivastava, C.K.P. Shinde, Chemosphere 90 (2013) 2254–2260.
[22] M. Verma, V.K. Gupta, V. Dave, R. Chandra, G.K. Prasad, J. Colloid Interface Sci. 438 (2015) 102–109.
[23] C.G. Granqvist, Sol. Energy Mater. Sol. Cells 60 (2000) 201–262.
[24] M. Sun, N. Xu, Y.W. Cao, J.N. Yao, E.G. Wang, J. Mater. Res. 15 (2000) 927–933.
[25] S. Supothina, P. Seeharaj, S. Yoriya, M. Sriyudthsak, Ceram. Int. 33 (2007) 931–936.
[26] C. Zhang, A. Boudiba, C. Navio, M.G. Olivier, R. Snyders, M. Debliquy, Sens. Actuat., B 161 (2012) 914–922.
[27] A. Boudiba, C. Zhang, P. Umek, C. Bittencourt, R. Snyders, M.G. Oliviera, M. Debliquy, Int. J. Hydrogen Energy 38 (2013) 2565–2577.
[28] J. Kukkola, M. Mohla, A.R. Leino, J. Mäklina, N. Halonena, A. Shchukarev, Z. Konya, H. Jantunen, K. Kordas, Sens. Actuat., B Chem. 186 (2013) 90–95.
[29] R. Abe, H. Takami, N. Murakami, B. Ohtani, J. Am. Chem. Soc. 130 (2008) 7780–7781.
[30] S. Anandana, T. Sivasankar, T.L. Villarreal, Ultrason. Sonochem. 21 (6) (2014) 1964–1968.
[31] C.P. Li, F. Lin, R.M. Richards, R.C. Tenent, C.A. Wolden, Sol. Energy Mater. Sol. Cells 121 (2014) 163–170.
[32] C. Pang, J. Luo, Z. Guo, M. Guo, T. Hou, Int. J. Refract. Met. Hard Mater. 28 (2010) 343–348.
[33] T.A. Nguyen, S. Park, J.B. Kim, T.K. Kim, G.H. Seong, J. Choo, Y.S. Kim, Sens. Actuat., B Chem. 160 (2011) 549–554.
[34] D.B.H. Uresti, D.S. Martínez, A.M. Cruz, S.S. Guzmán, L.M.T. Martínez, Ceram. Int. 40 (2014) 4767–4775.
[35] R. Chandra, P. Taneja, J. John, P. Ayyub, Nanostruct. Mater. 11 (8) (1999) 1171–1179.
[36] S. Ghosh, S.S. Acharyya, S. Adak, L.N.S. Konathala, T. Sasaki, R. Bal, Green Chem. 16 (2014) 2826–2834.
[37] X. Zhang, X. Lu, Y. Shen, J. Han, L. Yuan, L. Gong, Z. Xu, X. Bai, M. Wei, Y. Tong, Y. Gao, J. Chen, J.Z. Zhong, L. Wang, Chem. Commun. 47 (2011) 5804–5806.
[38] A.K. Chawla, R. Chandra, J. Nanopart. Res. 11 (2009) 297–302.
[39] D.S. Martínez, A.M. Cruz, E.L. Cuellar, Mater. Res. Bull. 48 (2013) 691–697.
[40] A.M. Cruz, D.S. Martínez, E.L. Cuéllar, Solid State Sci. 12 (2010) 88–94.
[41] J. Cao, B. Luo, H. Lin, B. Xu, S. Chen, Appl. Catal. B 111–112 (2012) 288–296.
[42] K.J. Laidler, Chemical Kinetics, McGraw-Hill Book Company Inc, New York, 1950.
[43] G.K. Prasad, T.H. Mahato, B. Singh, K. Ganesan, P. Pandey, K. Sekhar, J. Hazard. Mater. 149 (2007) 460–464.
[44] S. Rajagopalan, O. Koper, S. Decker, K.J. Klabunde, Chem. Eur. J. 8 (2002) 2602–2607.
[45] G.W. Wagner, L.R. Procell, R.J. O'Connor, M. Shekar, C.L. Carnes, P.N. Kapoor, K.J. Klabunde, J. Am. Chem. Soc. 123 (2001) 1636–1644.
[46] G.K. Prasad, T.H. Mahato, B. Singh, P. Pandey, A.N. Rao, K. Ganesan, R. Vijayraghavan, AICHE J. 53 (6) (2007) 1562–1567.
[47] X. Gu, J. Ge, H. Zhang, A. Auroux, J. Shen, Thermochim. Acta 451 (2006) 84–93.
[48] H. Tang, Z. Cheng, H. Zhu, G. Zuo, M. Zhang, Appl. Catal. B: Environ. 79 (2008) 323–333.
[49] T.H. Mahato, B. Singh, A.K. Srivastava, G.K. Prasad, A.R. Srivastava, K. Ganesan, R. Vijayaraghavan, J. Hazard. Mater. 192 (2011) 1890–1895.
[50] Y.C. Yang, J.A. Baker, J.R. Ward, Chem. Rev. 92 (1992) 1729–1743.
[51] T.H. Mahato, G.K. Prasad, B. Singh, A.R. Srivastava, K. Ganesan, J. Acharya, R. Vijayaraghavan, J. Hazard. Mater. 166 (2009) 1545–1549.
[52] A. Saxena, B. Singh, A. Sharma, V. Dubey, R.P. Semwal, M.V.S. Suryanarayana, V.K. Rao, K. Sekhar, J. Hazard. Mater. B134 (2006) 104–111.
[53] V.K. Gupta, R. Jain, A. Mittal, S. Agarwal, S. Sikarwar, Mater. Sci. Eng.: C 32 (2012) 12–17.
[54] T.A. Saleh, V.K. Gupta, Environ. Sci. Pollut. Res. 19 (2012) 1224–1228.
[55] V.K. Gupta, S.K. Srivastava, D. Mohan, S. Sharma, Waste Manage. 17 (1998) 517–522.
[56] V.K. Gupta, A. Mittal, J. Mittal, J. Colloid Interface Sci. 342 (2010) 518–527.
[57] V.K. Gupta, A. Mittal, D. Kaur, A. Malviya, J. Mittal, J. Colloid Interface Sci. 337 (2009) 345–354.
[58] A. Mittal, A. Malviya, J. Mittal, V.K. Gupta, J. Colloid Interface Sci. 340 (2009) 16–26.
[59] V.K. Gupta, S. Agarwal, T.A. Saleh, J. Hazardous Mat. 185 (2011) 17–23.
[60] V.K. Gupta, I. Ali, T.A. Saleh, A. Nayak, S. Agarwal, RSC Advances 2 (2012) 6380–6388.
[61] V.K. Gupta, A. Mittal, J. Mittal, J. Colloid Interface Sci. 344 (2010) 497–507.
[62] V.K. Gupta, R. Jain, S. Agarwal, M. Shrivastava, Mater. Sci. Eng.: C 31 (2011) 1062–1067.
[63] V.K. Gupta, A. Nayak, Chem. Eng. J. 180 (2012) 81–90.
[64] T.A. Saleh, V.K. Gupta, J. Colloids Interface Sci. 371 (2012) 101–106.
[65] H. Khani, M.K. Rofouei, P. Arab, V.K. Gupta, Z. Vafaei, J. Hazardous Materials 183 (2010) 402–409.
[66] R. Jain, V.K. Gupta, N. Jadon, K. Radhapyari, Anal. Biochem. 407 (2010) 79–88.